Supplementary materials for: The extremely shallow M_W 4.9 2019 Le Teil earthquake, France: Main ground motion features and comparison with ground motion models

This supplementary material contains a description of the signal processing applied to each record (Text S1), a table (S1) that summarized the main characteristics of the different GMMs used in this study and 23 figures (S2-S24) that complement the various analyses presented in the main paper. References are provided at the end of the document. The dataset used in this study, containing metadata and ground-motion parameters from the Le Teil earthquake records, is provided as an Excel table in the supplementary material.

1. Text S1: Signal processing

The usable frequency band (fmin-fmax) has been defined using the signal-to-noise ratio (SNR). With this aim, the signal and the noise time windows are defined by applying the algorithm of Perron *et al.* (2018) for window picking. For each selected time windows (signal and noise), detrending correction, 5% cosine taper, and zeros padding on each side of the windows are applied. Then the Fourier amplitude acceleration spectra (FAS) are computed and smoothed following to the Konno & Ohmachi (1998) algorithm with b=40. Finally, the usable bandwidth is determined by selecting frequencies where the FAS has a SNR greater than three. A further test consists in verifying that the amplitude of FAS has a shape consistent with the ω^2 decay (Brune, 1970) at low frequency. The seismic signals are band-pass filtered using a Butterworth acausal filter of the second order between fmin and fmax. Finally, the shape of the acceleration, velocity, and displacement signals are inspected to check the absence of linear trends, if it is the case the high-pass filter corner frequencies is increased. In the case of SNCF data, noise windows could not be identified (late triggering) and thus the SNR could not be computed. For these stations, we set fmin equal to 0.1 Hz, this value is eventually adjusted by checking the absence of linear trend in the displacement signal as described so far. Figure S.1 displays the usable frequency band (fmin-fmax) defined in this study.

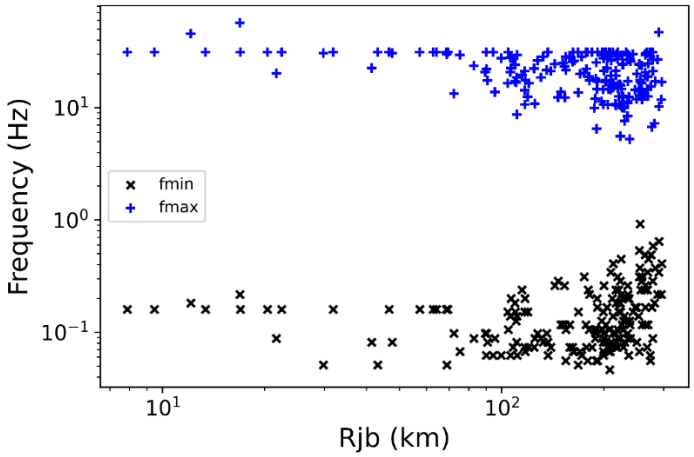

Figure S.1. Suggested usable frequencies according to the Joyner-and-Boore distance defined in this study for each site.

2. Tables

Table S.1. Main characteristics of the different GMMs used in this study.

Reference	**Code**	**Region of database**	**Source parameters**	***MW* range**	**Distance (km)**	**Period range (s)**	**Horizontal component definition**
Boore *et al.* (2014)	Bo14	Global	M_W, mech	3.0-8.5	$R_{JB} \leq 400$	0.01 – 10	RotD50
Chiou and Youngs, (2014)	CY14	Global	M_W, dip, Z_{TOR}, mech, R_{JB}, R_{RUP}, R_x	3.5-8.0	$R_{RUP} \leq 300$	0.01 – 10	RotD50
Bindi *et al.* (2014)	Bi14	Europe	M_W, mech	4.0-7.6	$R_{JB} \leq 300$	0.02 – 3	GM
Cauzzi *et al.* (2015)	Ca15	Global	M_W, mech	4.5-8.5	$R_{RUP} \leq 150$	0.01 – 10	GM
Kotha *et al.* (2020)	Ko20	Europe	M_W, D_{HYPO}	3.0-7.4	$R_{JB} \leq 545$	0.01 – 8	RotD50

GM=geometric mean; RotD50=the median single-component horizontal ground motion across all non-redundant azimuths; mech = style of faulting; Z_{TOR}= depth to top of rupture; R_{RUP} = closest distance to the rupture plane; R_{JB} = Horizontal distance to the surface projection of the rupture (Joyner-Boore distance); *Rx* = Horizontal distance to top edge of rupture measured perpendicular to the strike (site coordinate).

3. Figures

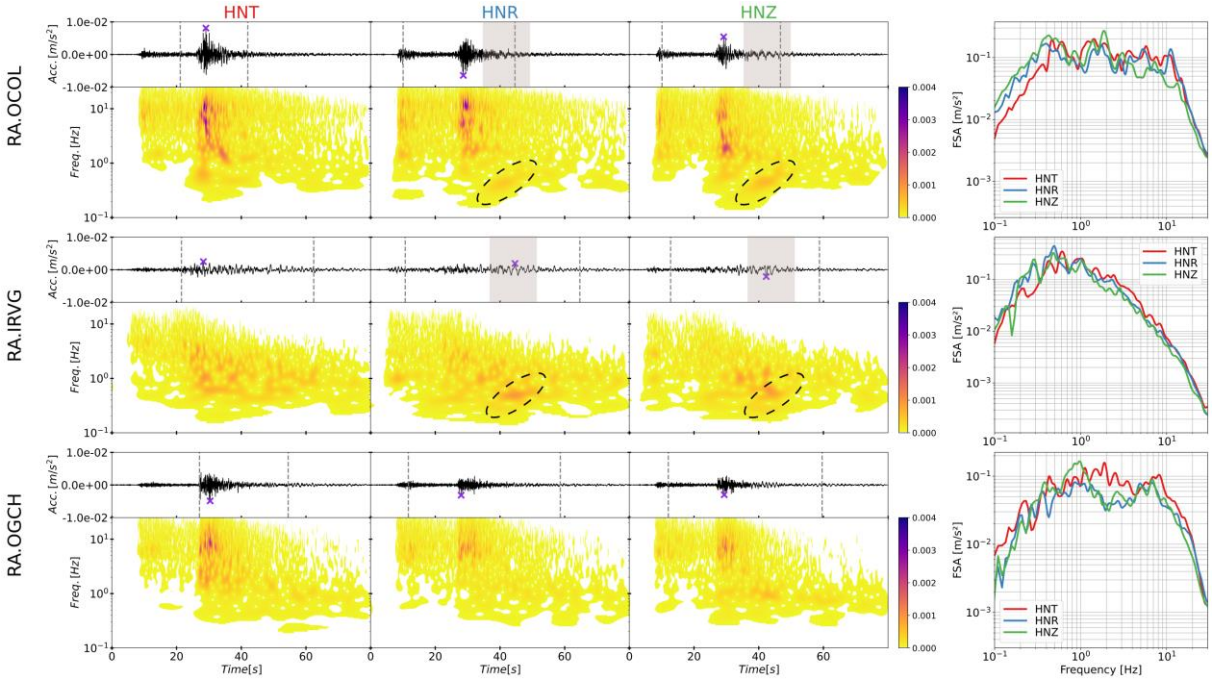

Figure S.2. Waveforms in acceleration, the corresponding Stockwell transform and the Fourier spectra in acceleration for the OCOL (located at the northwest), IRVG (located at the southeast) and OGCH (located at the northeast) stations for the transverse (in red), radial (in blue) and vertical (in green) components. The location of the three stations is given in Figure 2. For OCOL and IRVG stations, the presence of Rayleigh waves is indicated by grey rectangles on the waveforms and by dotted lines on the Stockwell transforms. On the waveforms, the purple cross indicates the PGA and the grey vertical dotted lines indicate the significant relative duration ($D_{SR\text{-}5\text{-}95\%}$).

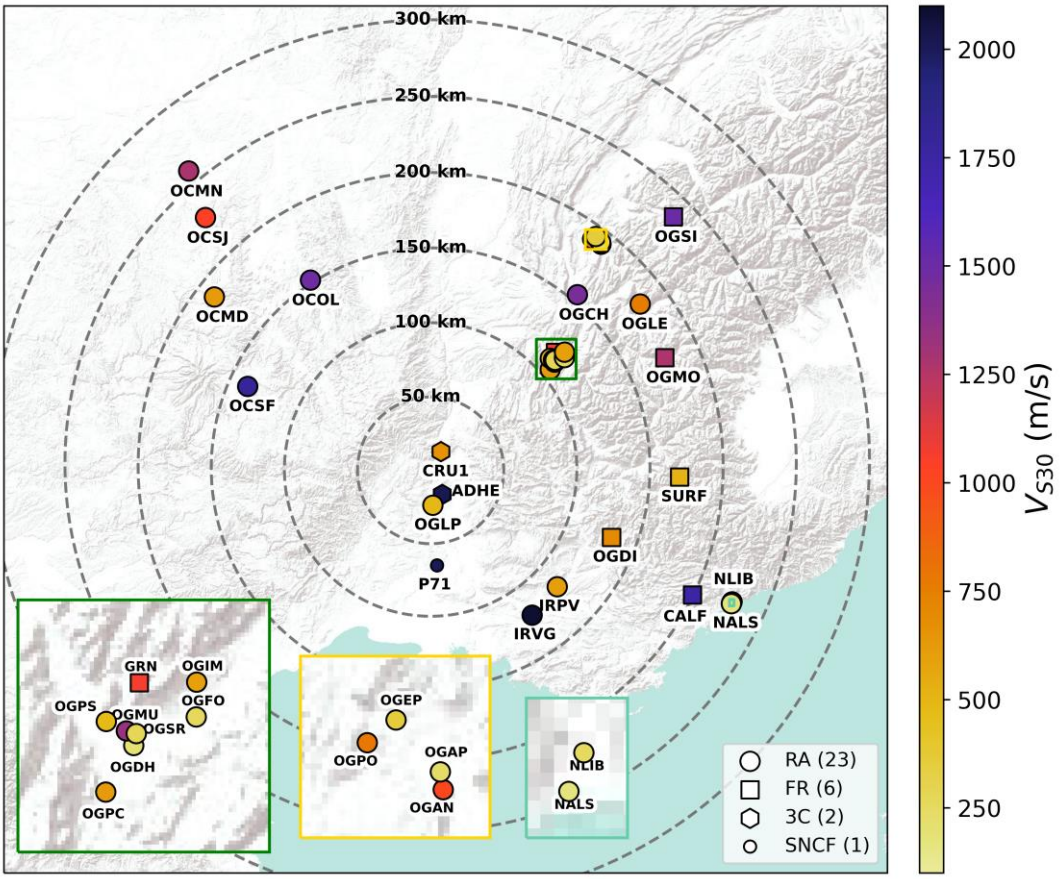

Figure S.3. Map of the stations associated to a V_{S30} value around the Le Teil earthquake, with a zoom around the cities of Grenoble, Annecy and Nice where several stations are deployed to characterize site effects in sedimentary basins.

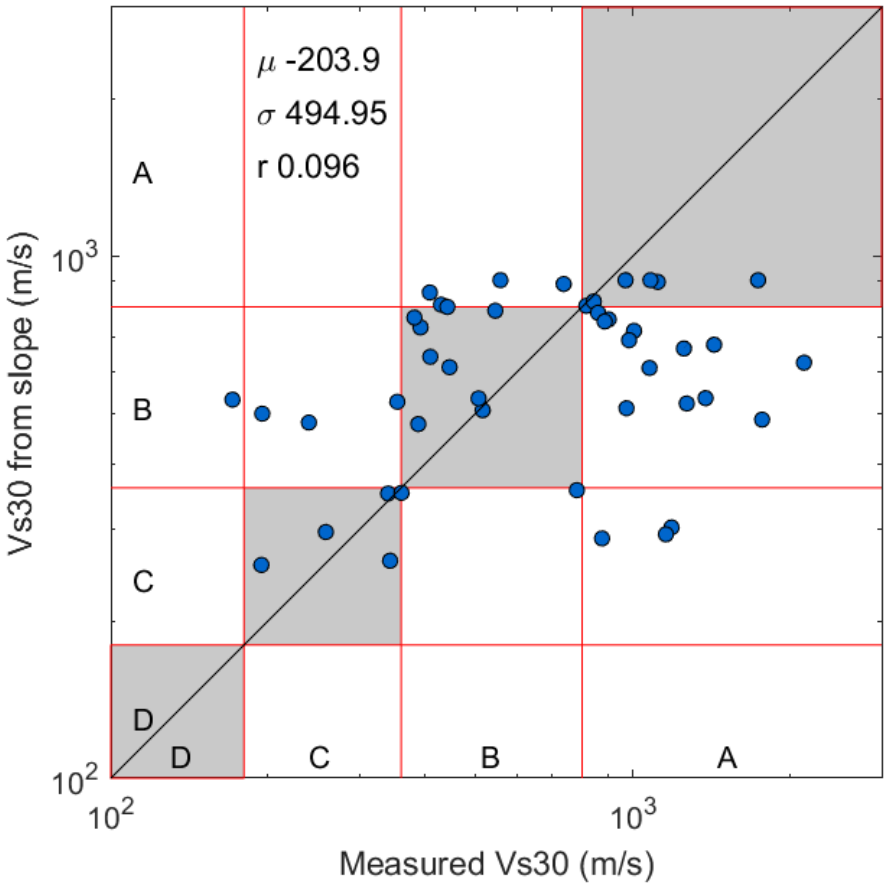

Figure S.4. Comparison between measured V_{S30} values at 47 sites *(Hollender* et al.*, 2018)*) and V_{S30} estimates derived from topographic slope using the ESHM20 site model (https://gitlab.seismo.ethz.ch/efehr/esrm20_sitemodel/). The black line represents the 1:1 identity line. Soil classes according to the EC8 classification are indicated, and grey boxes highlight sites for which the EC8 class remains unchanged between the two estimates. The mean (μ) and standard deviation (σ) of the differences between proxy and measured V_{S30} values are shown, along with the Pearson correlation coefficient (r).

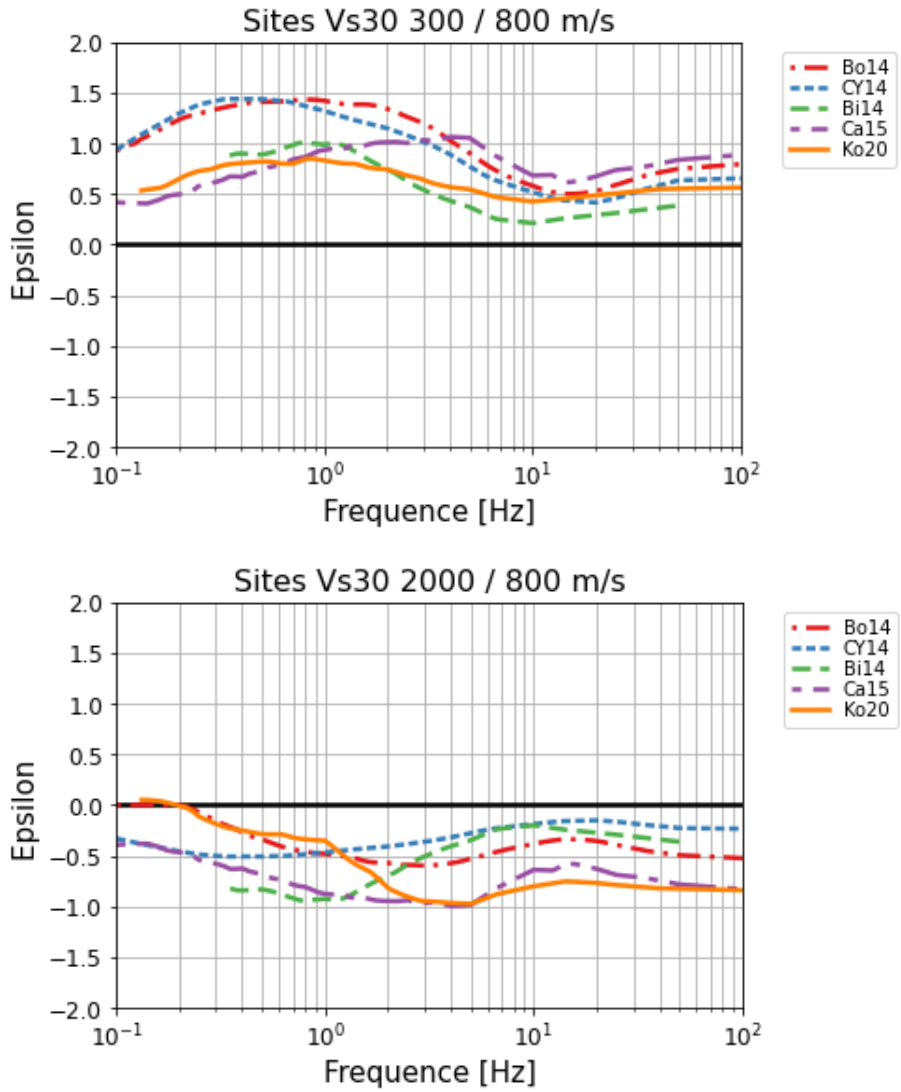

Figure S.5. Illustration of the impact of site condition (V_{S30}) on predicted ground motions in terms of normalized residuals. Residuals are computed as Res=[ln(Pred(V_{S30}-alt))-ln(Pred(V_{S30}-ref))]/σ_tot, where Pred is the median ground motion prediction from the GMM and σ_tot is the total standard deviation of the model. The top panel shows results for an V_{S30}-alt of 300 m/s, and the bottom panel for 2000 m/s. This figure quantifies the potential bias introduced when assuming a uniform reference V_{S30} of 800 m/s.

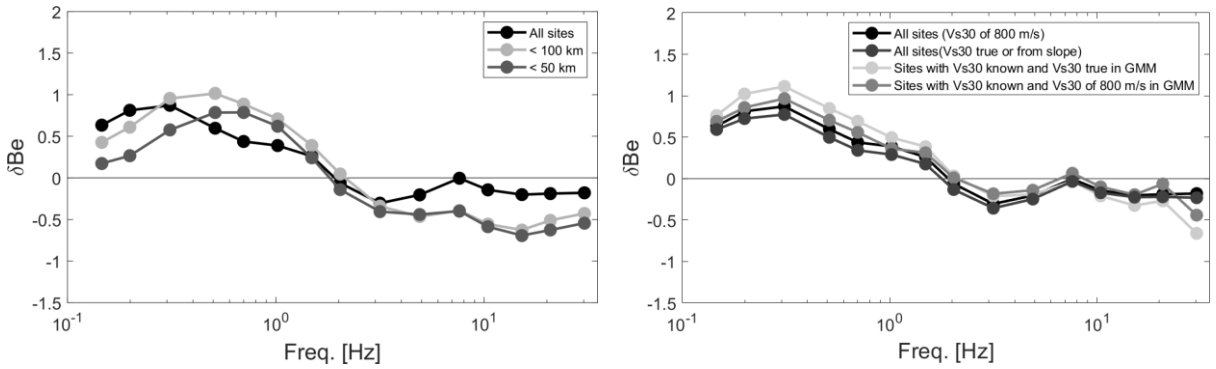

Figure S.6. Between-event residuals δB_e with respect to the frequency computed from Ko20 GMM and the selected dataset with the assumption of V_{S30}=800 m/s (all stations) and (left) using different subsets of stations based on their distance to the rupture and (right) (i) using measured V_{S30} where available and topographic-slope-based estimates *(Wald and Allen, 2007)* for the others and (ii) using the 32 stations for which V_{S30} is known for V_{S30}=800 m/s or the measured V_{S30} value in the GMM. Note that for each frequency, the number of stations used to compute δB_e varies according to the useable frequencies for each station.

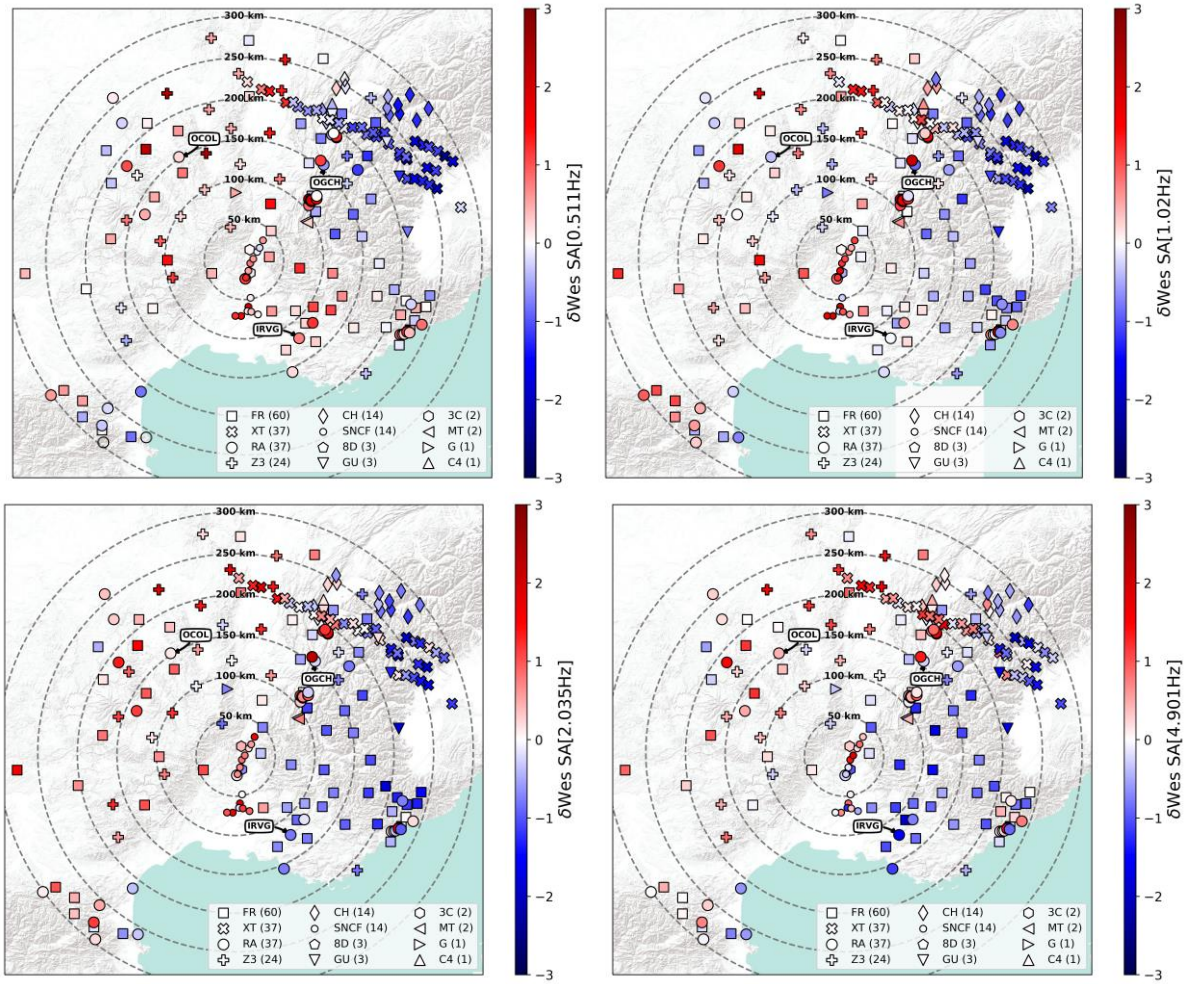

Figure S.7. Figure similar to Figure 7 using Bo14's GMM.

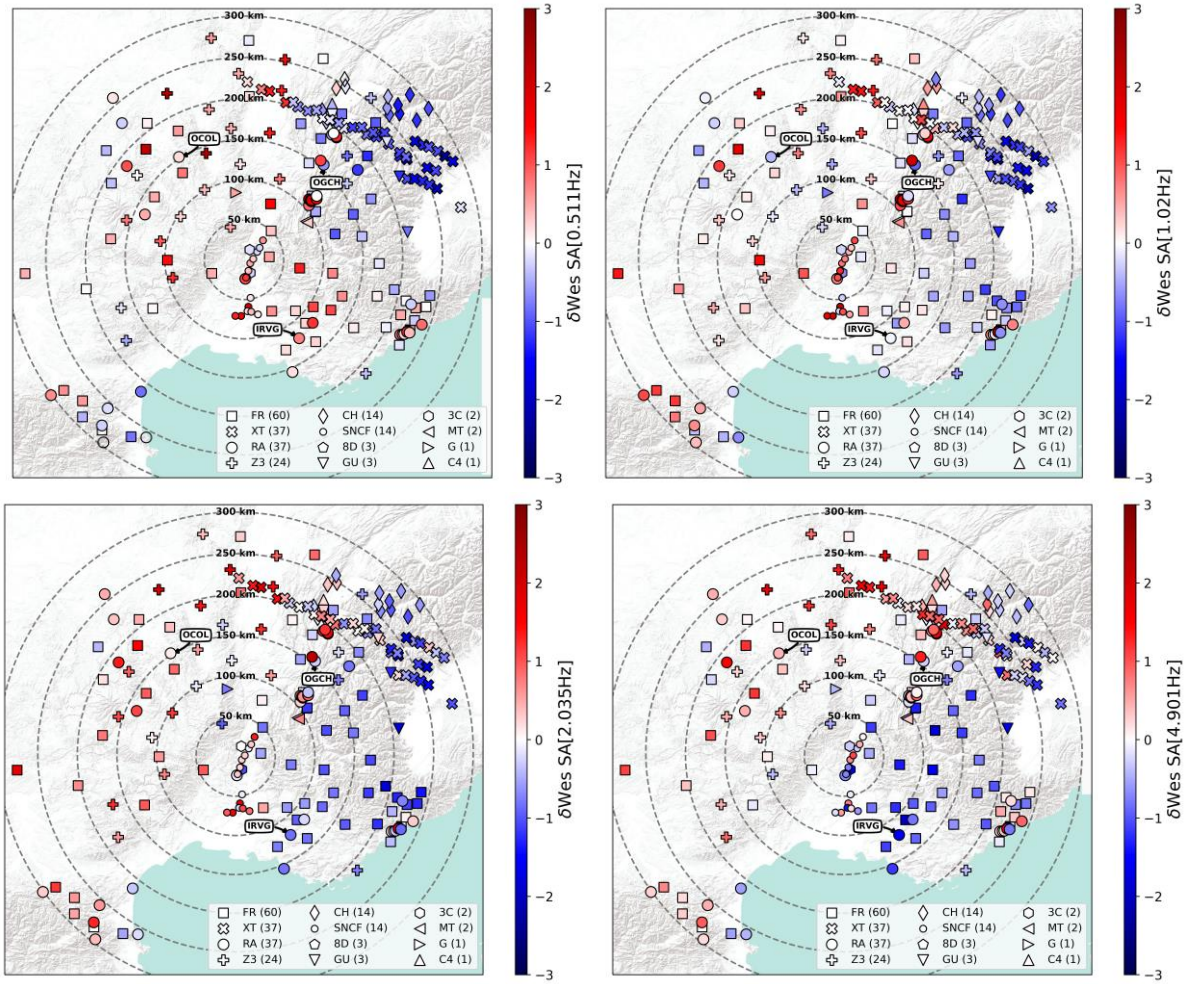

Figure S.8. Figure similar Figure 7 using CY14's GMM.

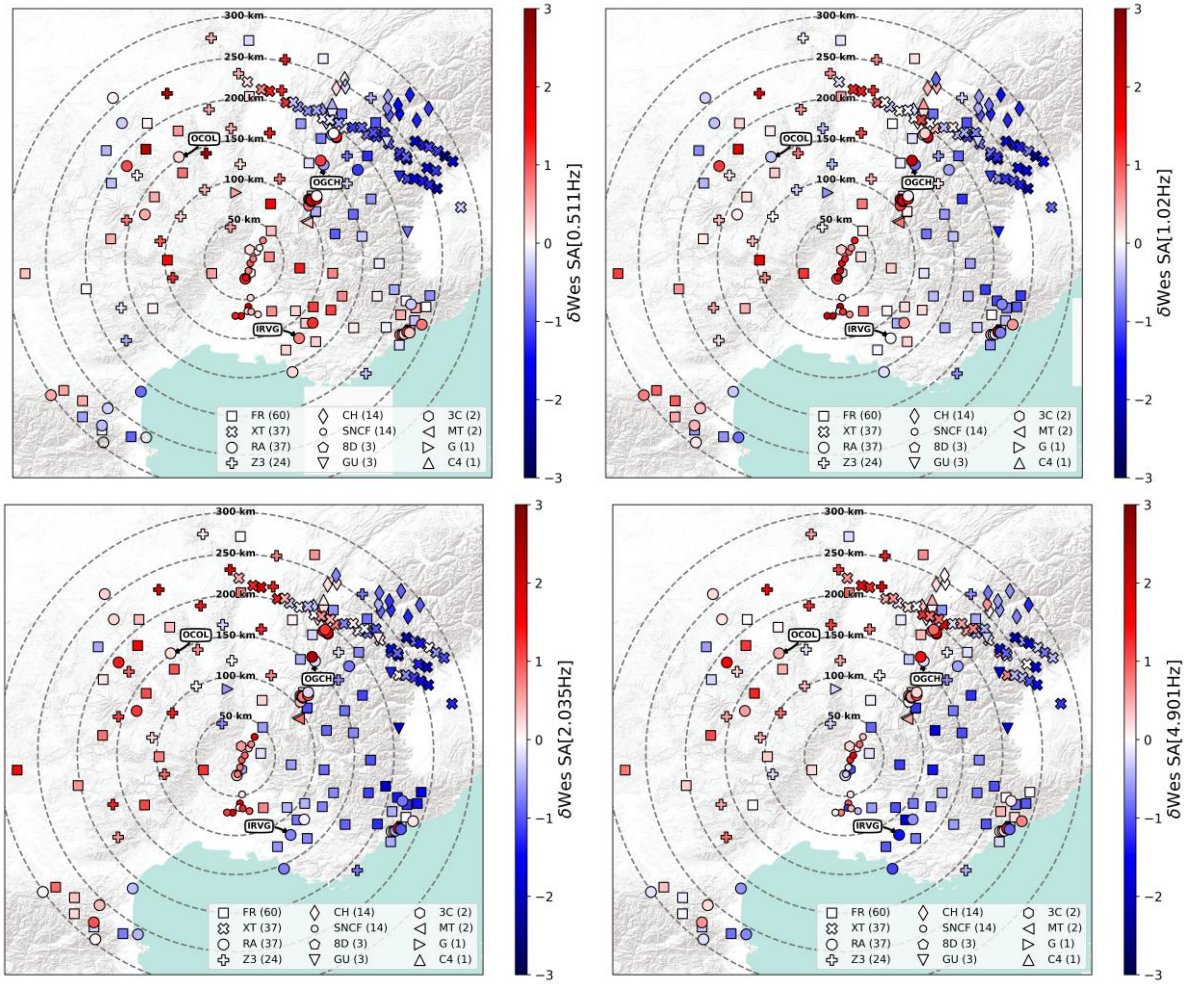

Figure S.9. Figure similar to Figure 7 using Bi14's GMM.

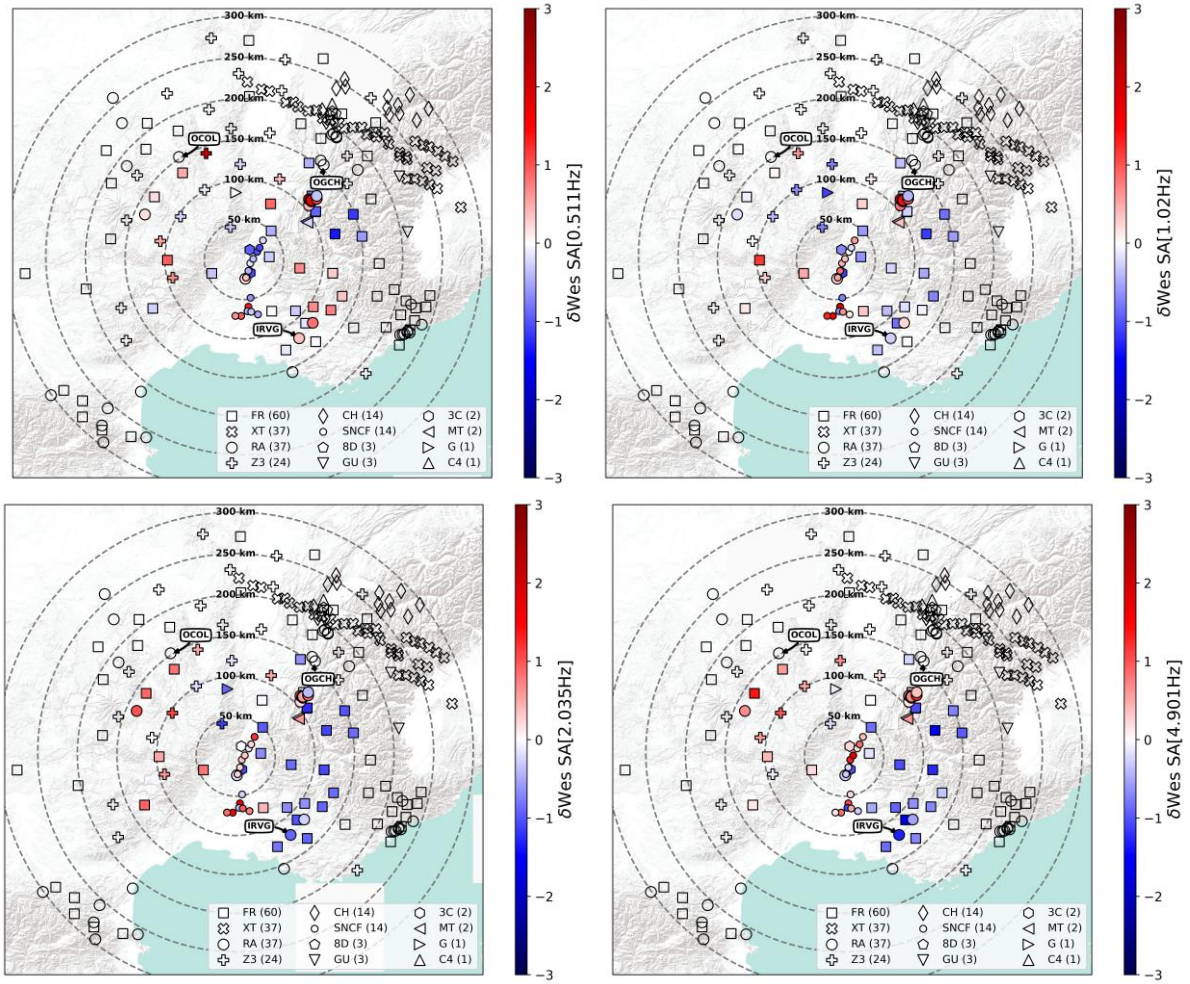

Figure S.10. Figure similar to Figure 7 using Ca15's GMM.

V_{S30} of 800 m/s

V_{S30} measured

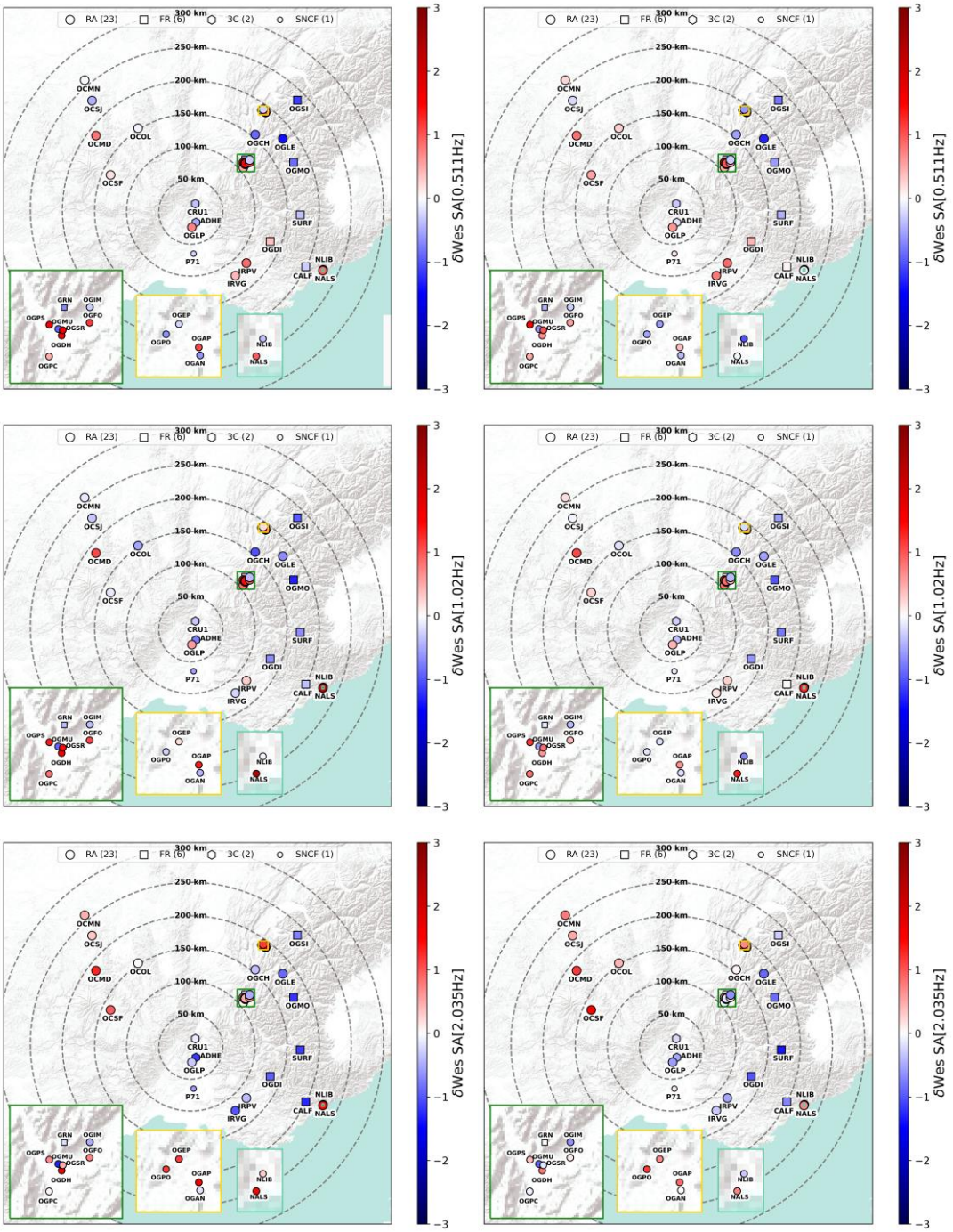

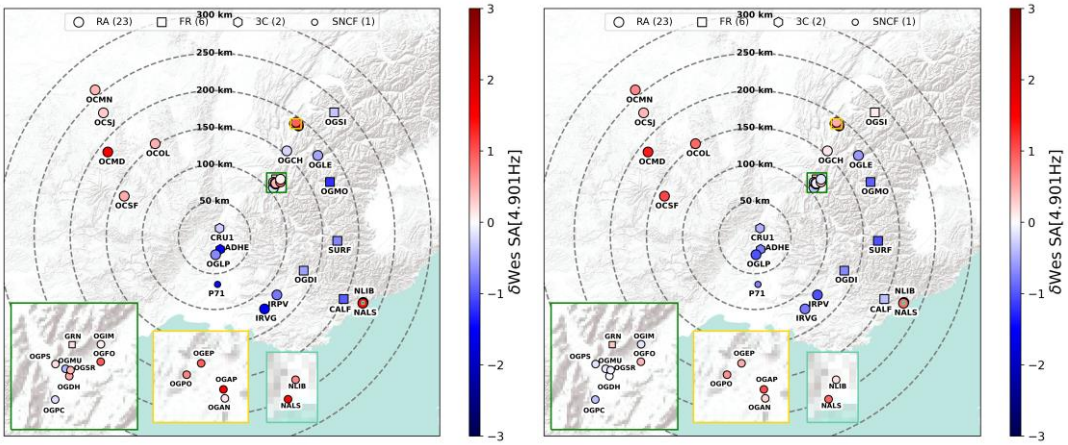

Figure S.11. Spatial distribution of within-event residuals (δW_{es}) computed using the Ko20's GMM for four frequencies only for the 32 stations for which V_{S30} is known (Figure S.3), under the assumption of V_{S30}=800 m/s (left panel) and using the measured V_{S30} value (right panel). The colour scale is limited to ±3 to emphasize differences; some data points fall outside these limits. For three areas, a zoom has been made to better visualize the data.

Vs30 of 800 m/s

Measured and slope-based Vs30

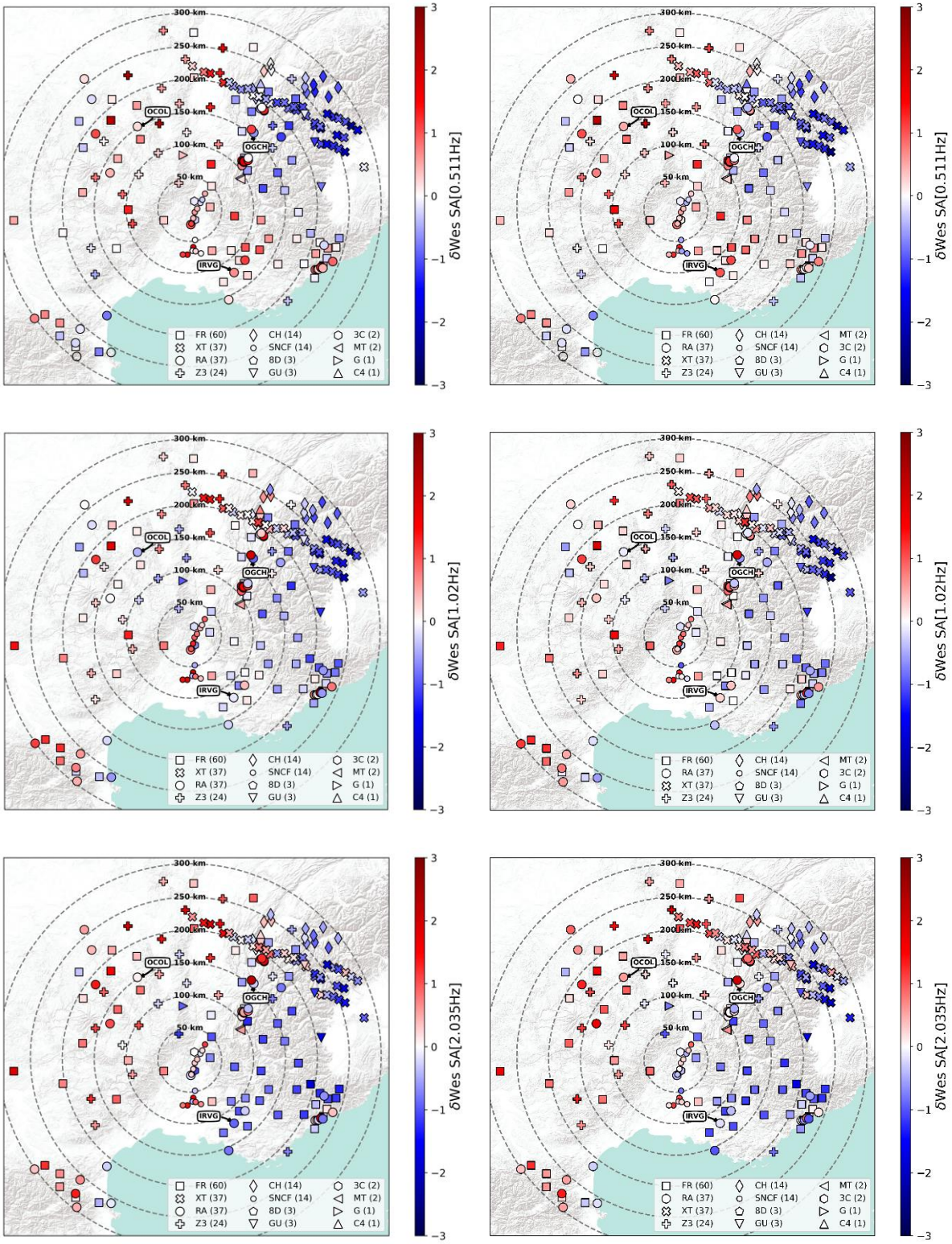

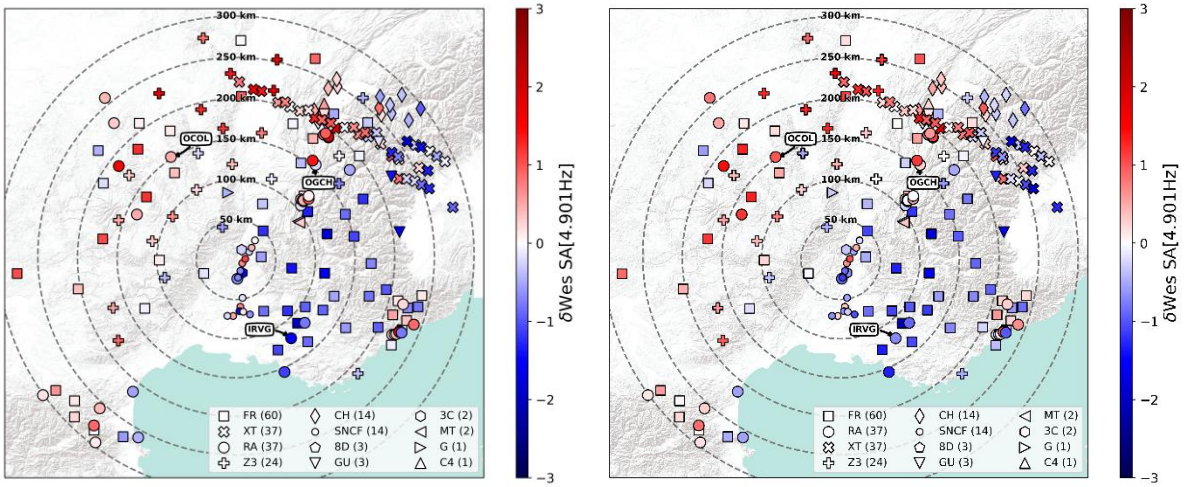

Figure S.12. Spatial distribution of within-event residuals (δW_{es}) computed using the Ko20's GMM for four frequencies, under the assumption of V_{S30}=800 m/s (left panel) and using the measured V_{S30} value for the 32 stations and then V_{S30} inferred from the topographic slope (right panel). The colour scale is limited to ±3 to emphasize differences; some data points fall outside these limits. For three areas, a zoom has been made to better visualize the data.

Ko20

Ko20 regional

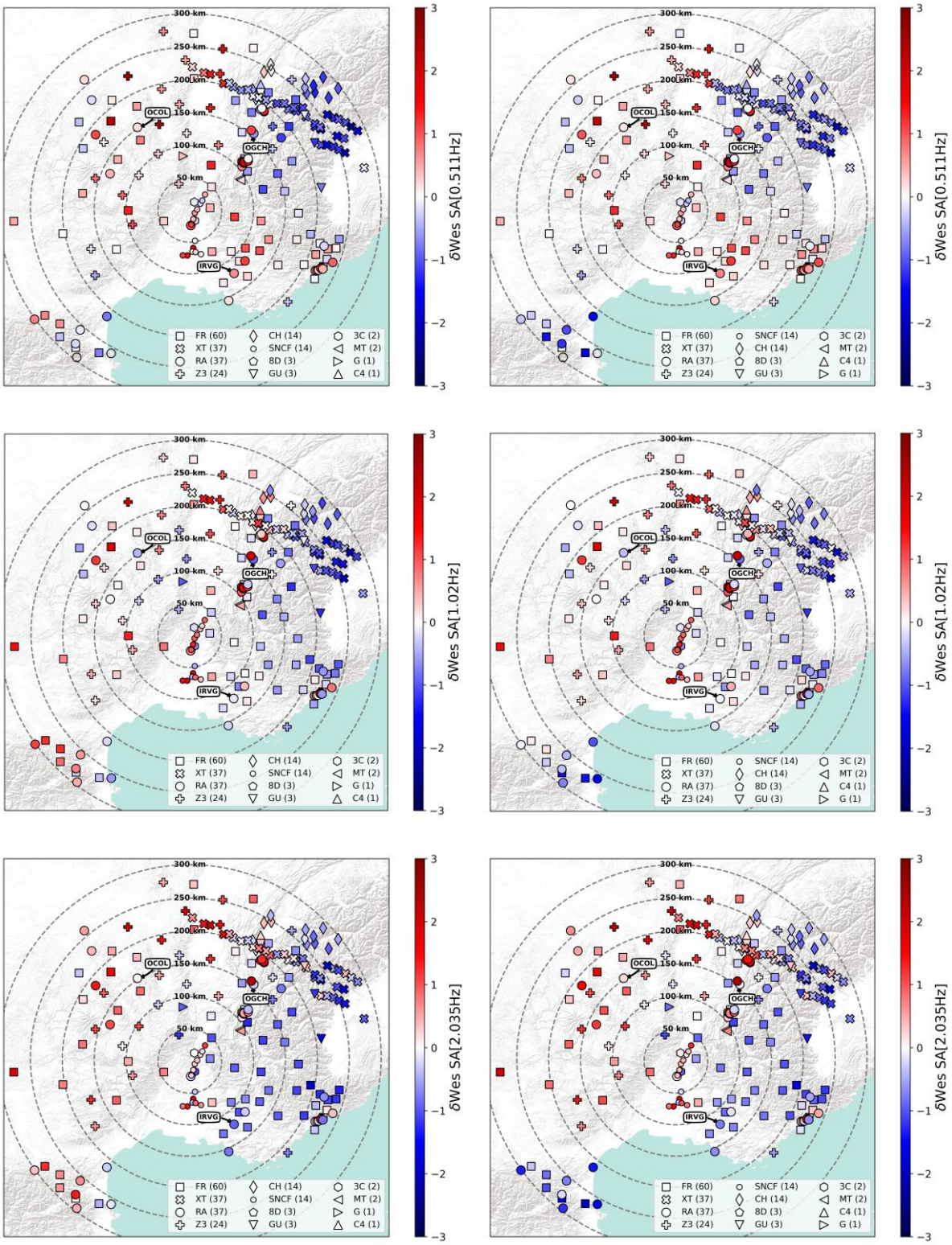

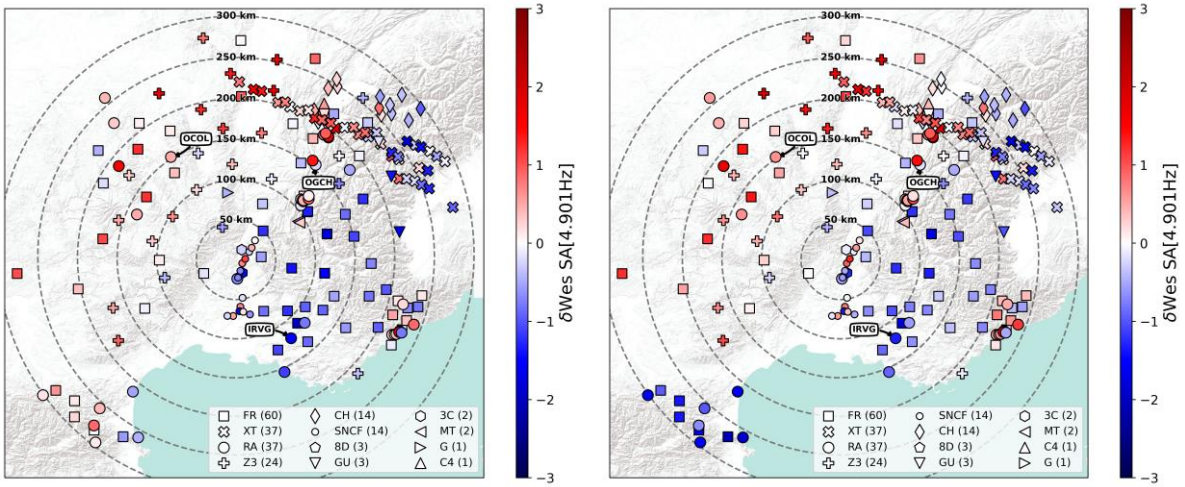

Figure S.13. Spatial distribution of within-event residuals (δW_{es}) computed using two versions of the Kotha et al. (2020)'s GMM under the assumption of V_{S30}=800 m/s: left panel, the median model used in this study and right panel, a regional model taking into account corrections due the location of the earthquake (δ_{L2L} source locality variability) and the location of each station (δ_{c3} attenuation variability). The colour scale is limited to ±3 to emphasize differences; some data points fall outside these limits.

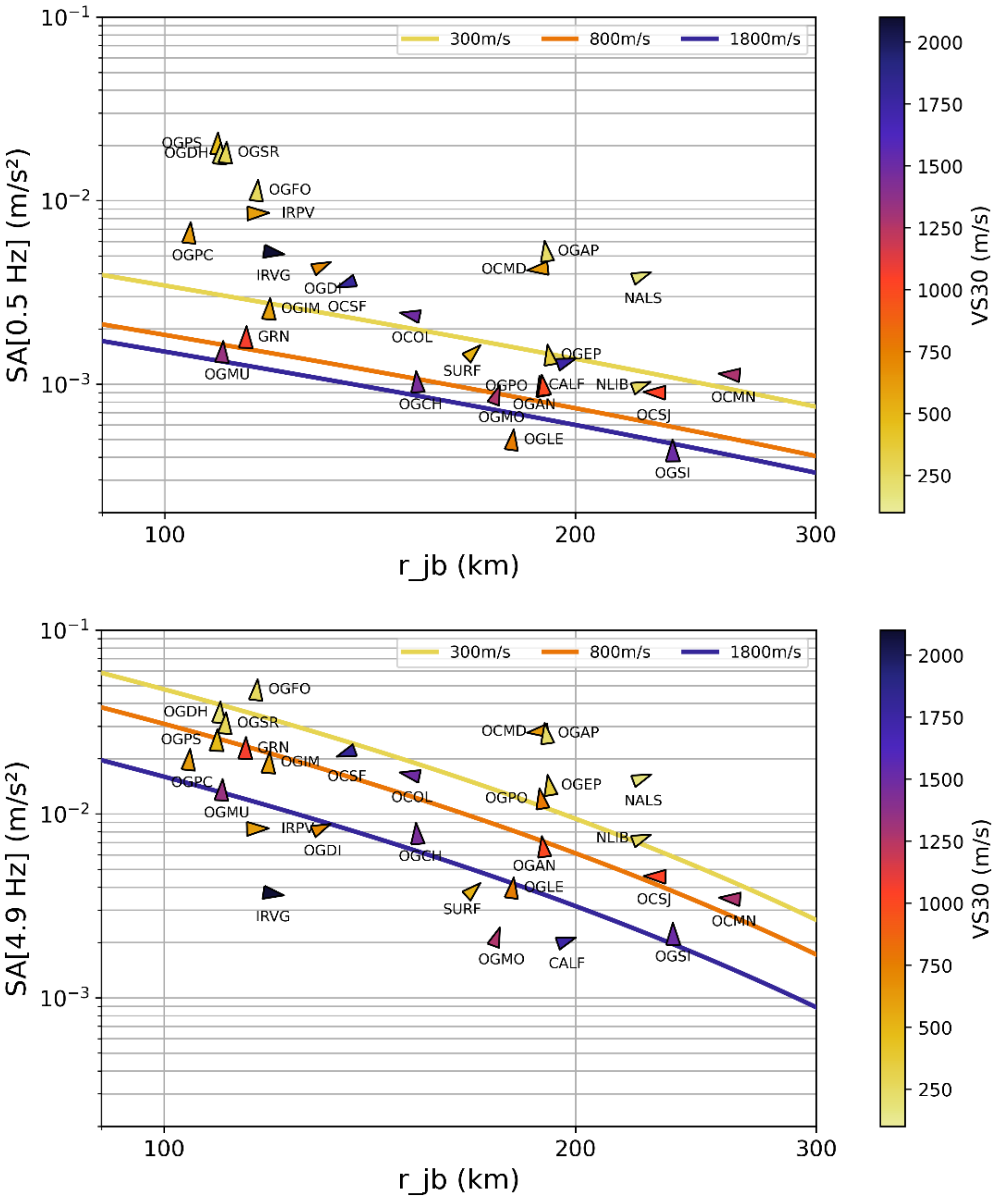

Figure S.14. Spectral acceleration (SA) in m/s^2 of the observations of the Le Teil earthquake defined in RotD50 compared to the Ko20's GMM for three V_{S30} values for 0.5 and 5 Hz. The peak of the triangle indicates the azimuth of the station with respect to the fault plane.

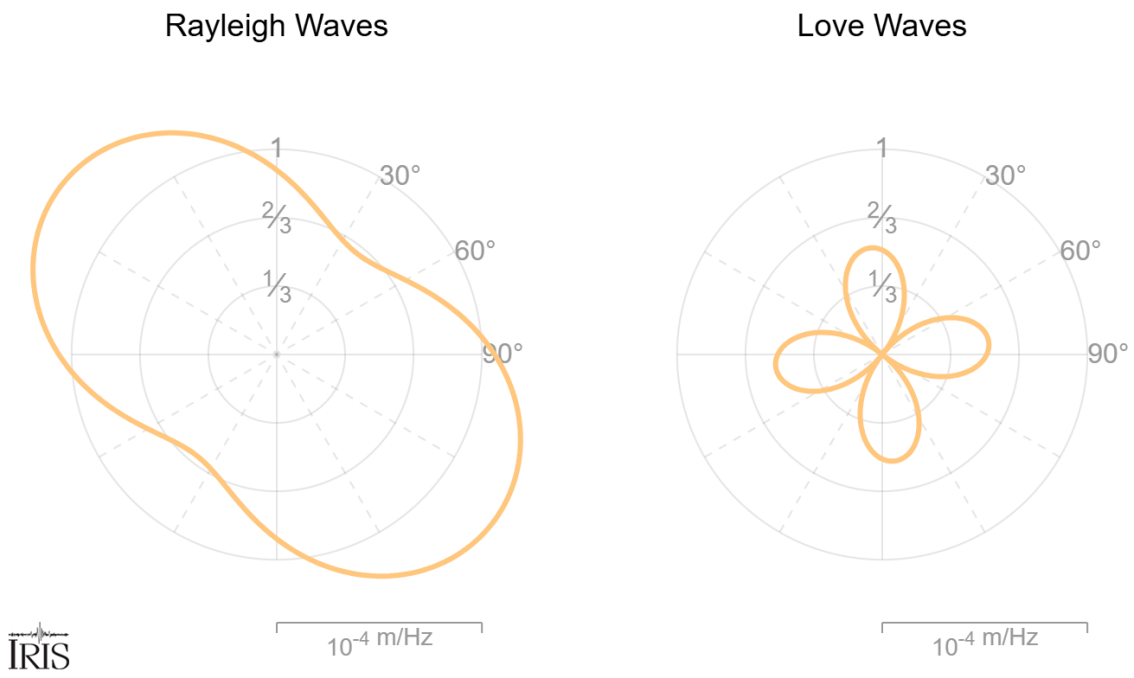

Figure S.15. Surface-wave radiation pattern for Rayleigh and Love waves at 0.06 Hz for the 2019 Le Teil earthquake, generated using the IRIS DMC tool (IRIS DMC, 2018). The radiation pattern illustrates the amplitude variation of surface waves as a function of azimuth. The representation is shown at 0.06 Hz, which corresponds to the highest frequency available in the tool. Reference: IRIS DMC (2018), Data Services Products: The Surface-Wave Radiation Patterns, https://doi.org/10.17611/DP/SWRP.1.

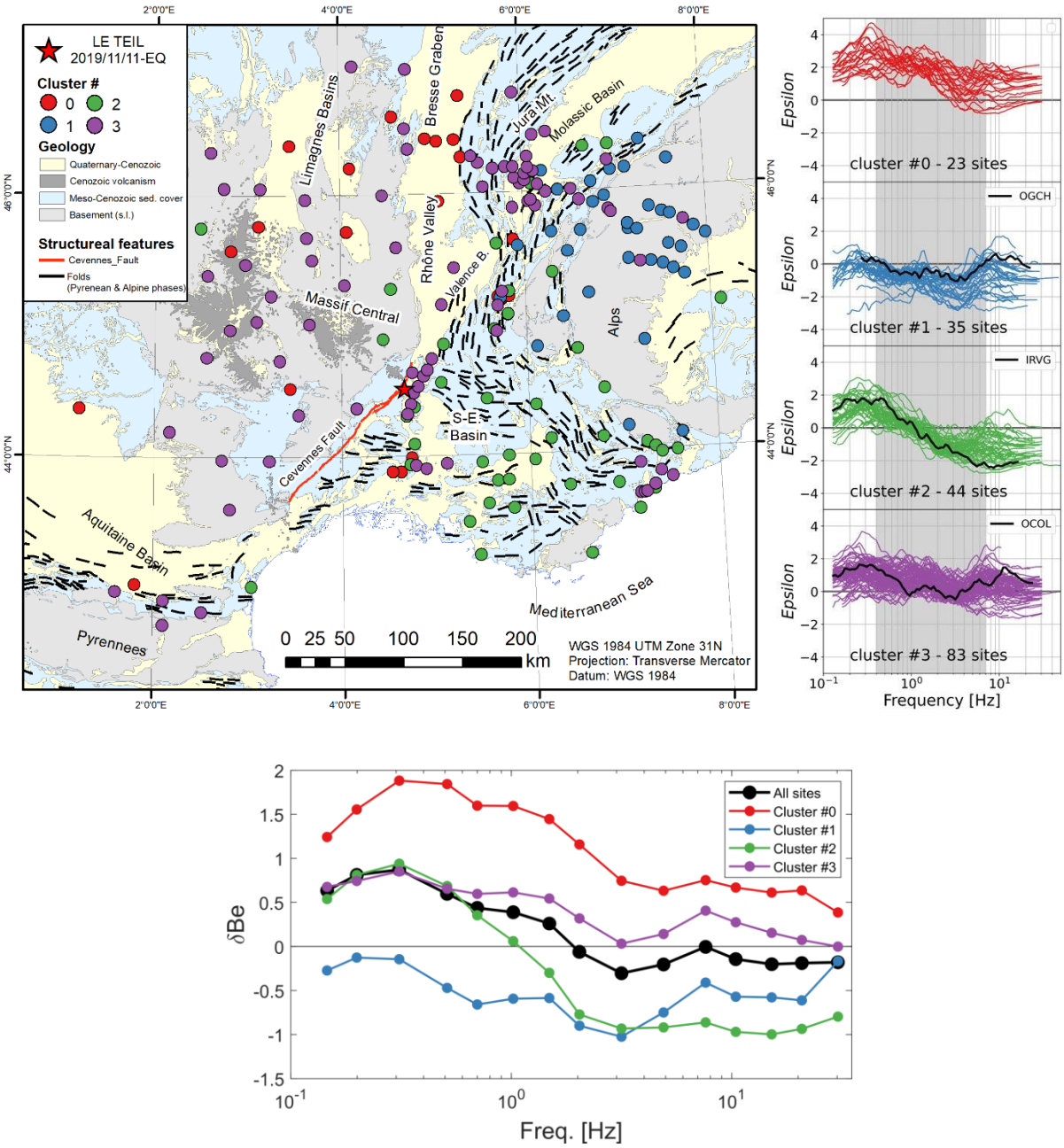

Figure S.16. Top figures similar to Figure 8 but applied to epsilon (see Equation 1) instead of the within-event term (see Equation 2). Bottom figure displays the between-event residuals with respect to the frequency using the stations of the four clusters represented on the top figure.

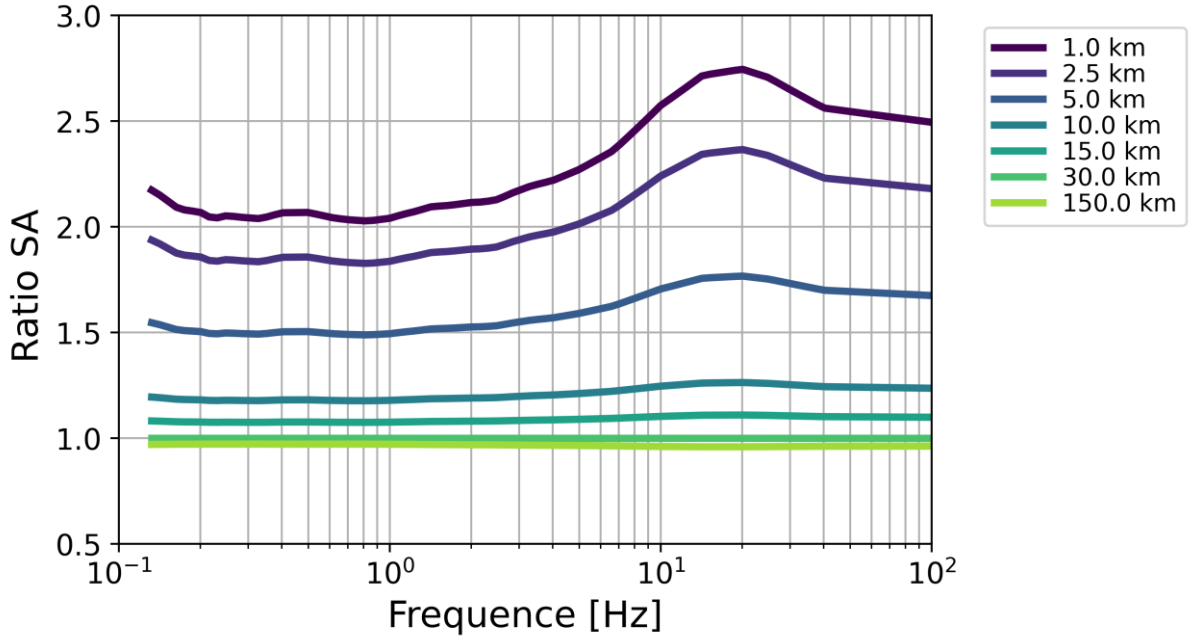

Figure S.17. Spectral ratios with respect to the frequency computed between the response spectra in acceleration (SA) predicted by the Ko20 GMM for the 0-10 km depth class and the 10-20 km depth class for different R_{JB} distances (in colour). The predicted spectra are computed using the parameters of the Le Teil earthquake (Table 1), except for the depth.

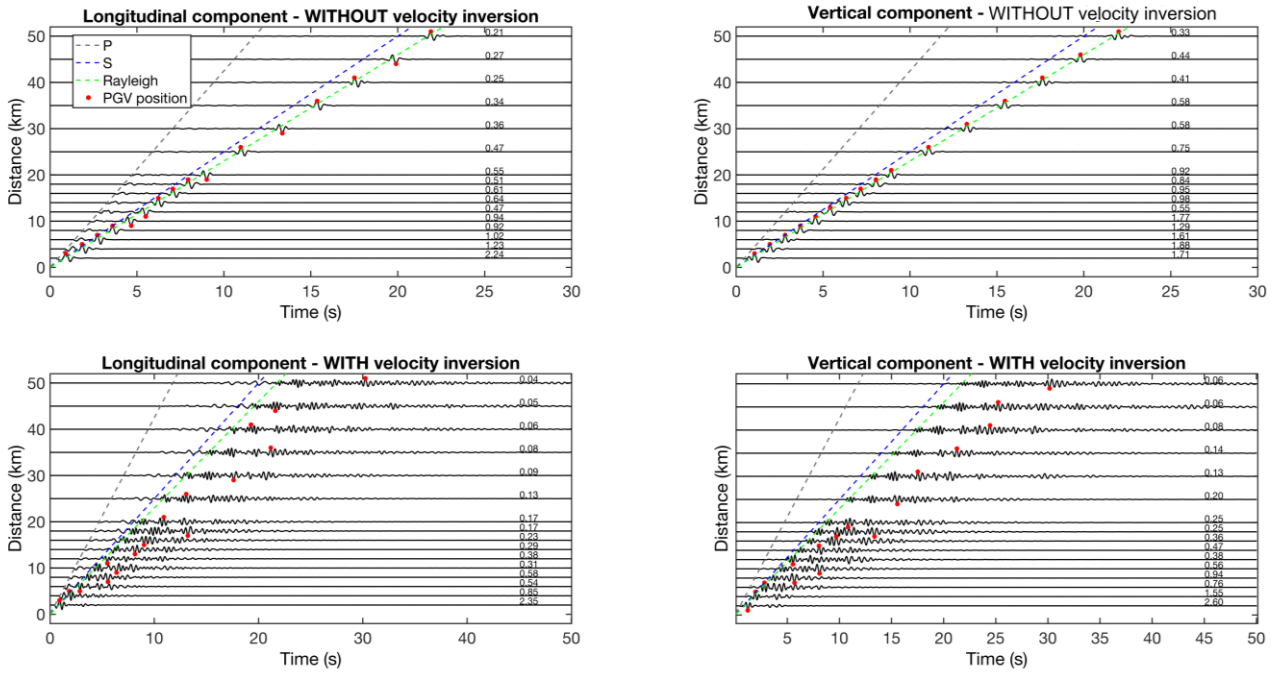

Figure S.18. Simulated surface acceleration time histories between 2 and 50 km for the velocity profiles of Figure10 (top: model with 2 elastic layers, bottom: model composed of 3 elastic layers in which the middle layer has the lowest velocity). The red dots indicate the peak ground acceleration, the values of which are given in m/s^2. The dashed lines represent various wave velocities (black: P wave, blue: S wave, green: Rayleigh wave).

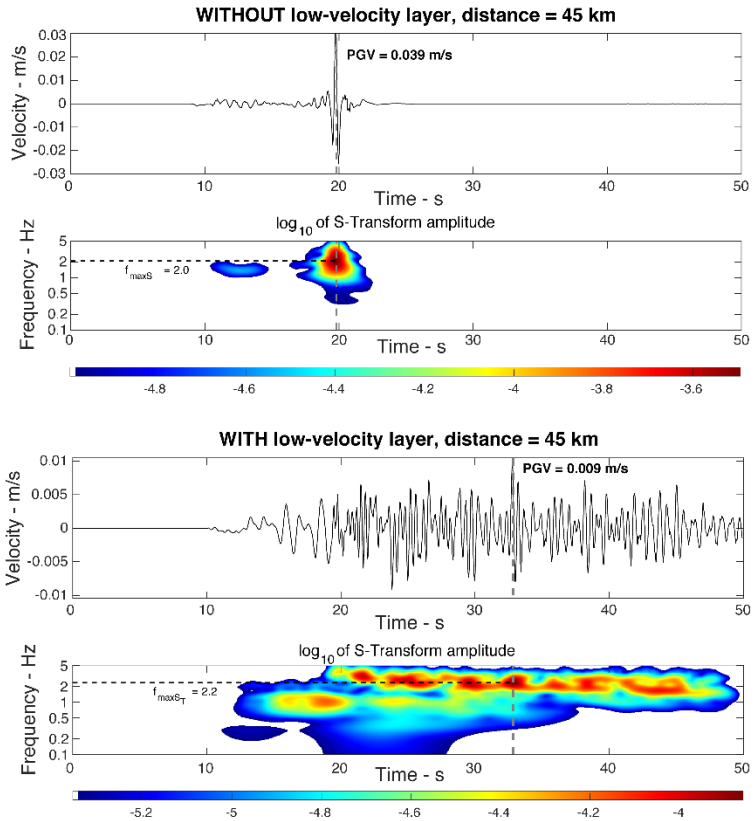

Figure S.19. Simulated ground velocity and Stockwell Transform at a distance of 45 km for the velocity profiles of Figure 10 (top: model with 2 elastic layers, bottom: model composed of 3 elastic layers in which the middle layer has the lowest velocity). The Peak Ground Velocity (PGV) and the frequency that controls the PGV (f_{maxST}) are indicated.

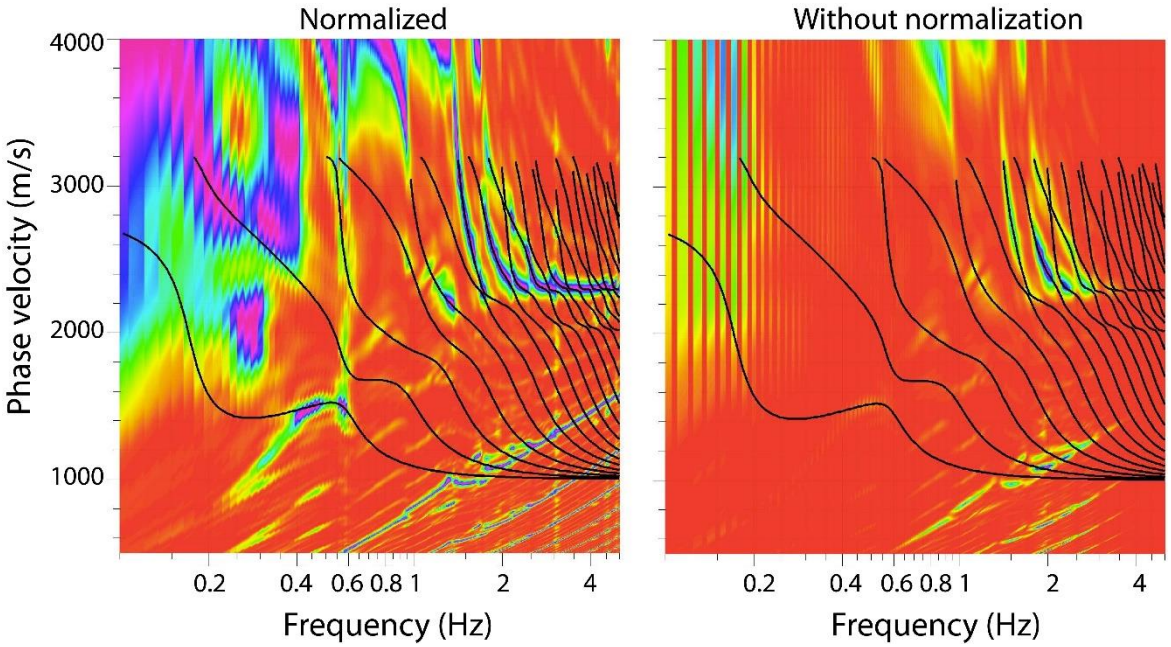

Figure S.20. Dispersion curves of the Rayleigh wave computed for the 1D-velocity model of Figure 10 with velocity inversion. The source depth is 0.5 km. Dispersion curves are calculated using a linear-frequency wavenumber algorithm using the GEOPSY software (Wathelet et al. 2018) (left: curves are normalized by the maximum beam power at each frequency; right: curves without normalization). The black curves represent the theoretical dispersion curves (first 20 normal modes) while the red to magenta colour relates to the minimum to the maximum beampower.

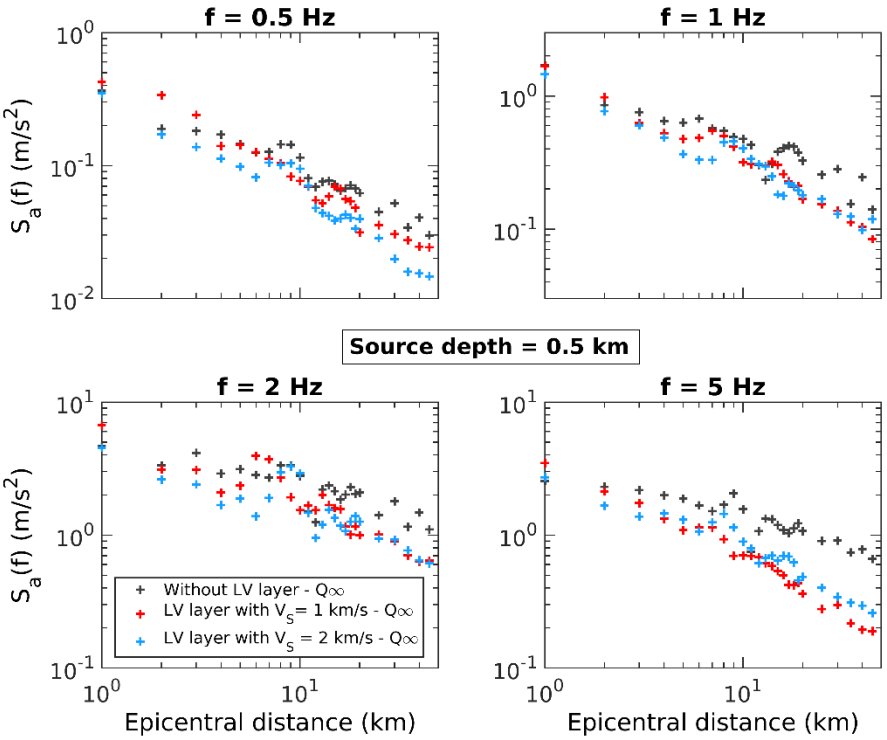

Figure S.21. Decrease of spectral acceleration Sa(f) with distance at various frequencies for the 1D-velocity media of Figure 10, without velocity inversion (in black), with the presence of a LV layer with V_S=1 km/s (in red) or V_S=2 km/s (in blue). The medium is purely elastic.

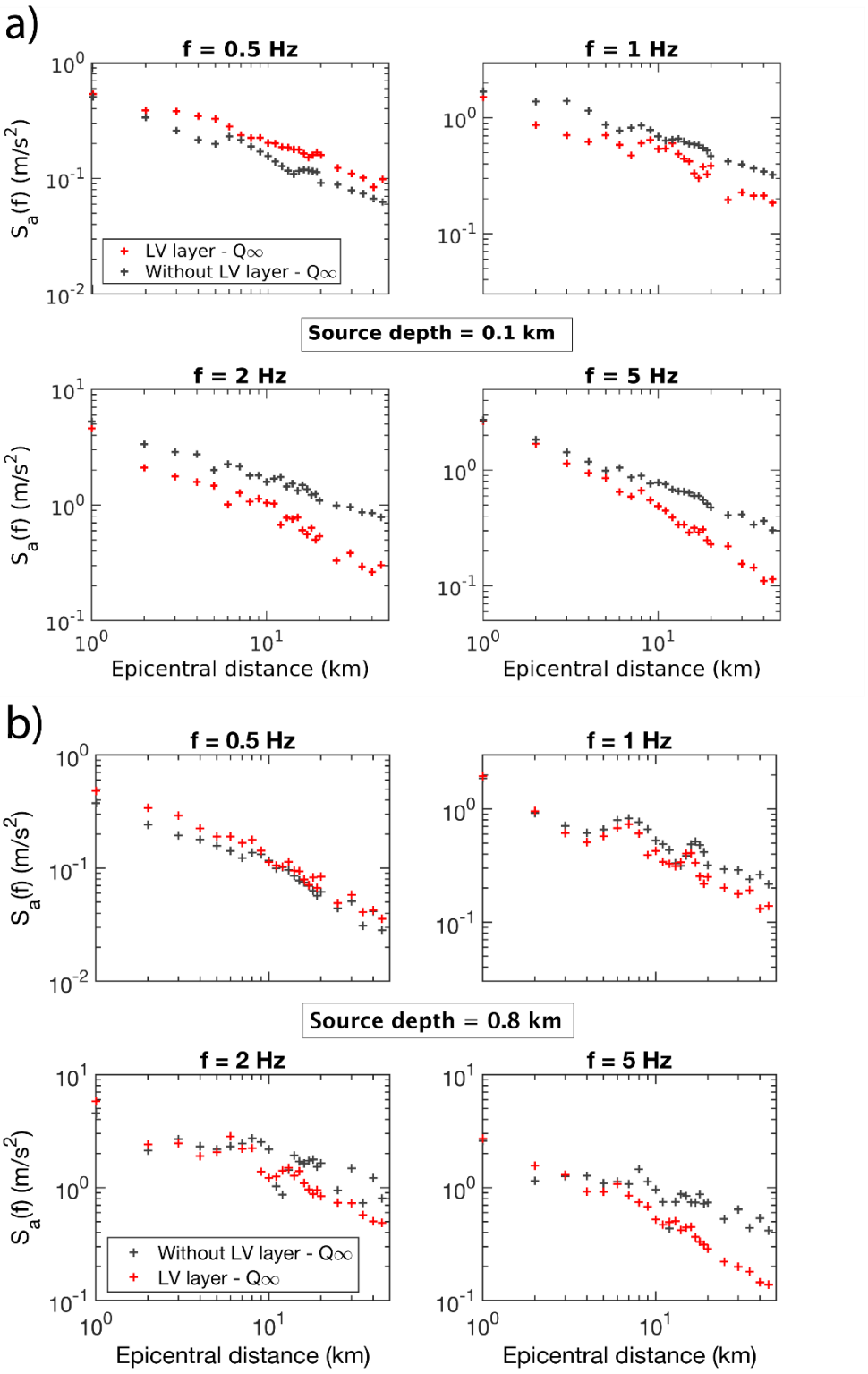

Figure S.22. Effect of the source depth on the decrease of spectral acceleration Sa(f) with distance at various frequencies for the 1D-velocity media of Figure 10, without velocity inversion (in black) and with the presence of a LV layer (in red). The medium is purely elastic.

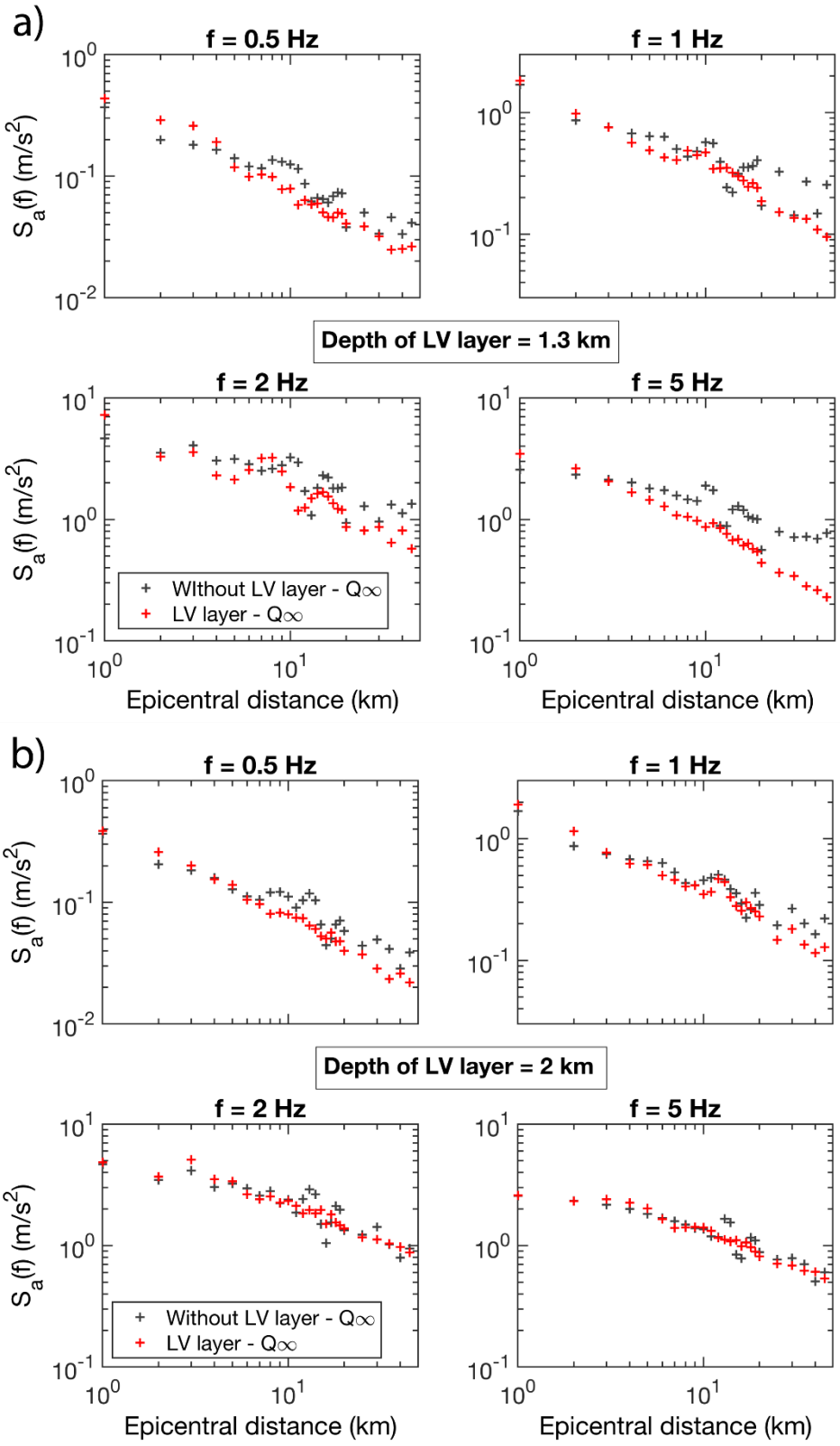

Figure S.23. Effect of the depth of the LV layer on the decrease of spectral acceleration Sa(f) with distance at various frequencies for 1D-velocity media similar to the one of Figure 10, but with deeper basement medium. The depths of the LV layers are then 1.3 km and 2 km (instead of 1 km). Black crosses: without velocity inversion; red crosses: with the presence of a LV layer. The medium is purely elastic.

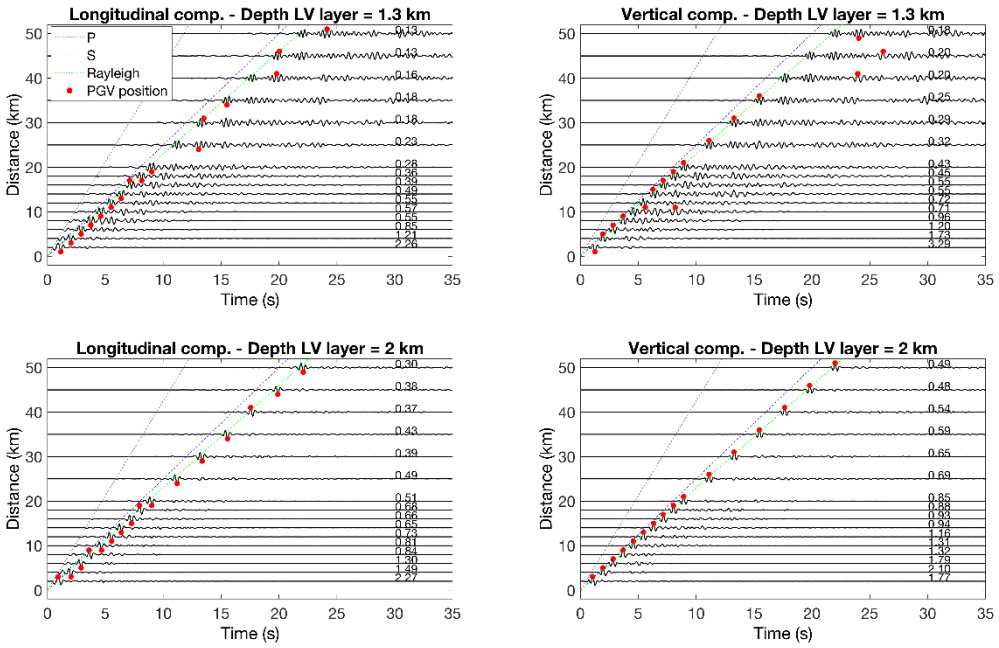

Figure S.24. Simulated surface acceleration time series between 2 and 50 km for velocity profiles composed of three elastic layers with a velocity inversion (similarly to Figure 10, dashed grey line), but which the low-velocity (LV) layer is buried at 1.3 km or 2 km. The red dots indicate the peak ground acceleration, the values of which are given in m/s^2. The dashed lines represent various wave velocities (black: P wave, blue: S wave, green: Rayleigh wave).

4. References

Bindi, D. *et al.* (2014) 'Pan-European ground-motion prediction equations for the average horizontal component of PGA, PGV, and 5 %-damped PSA at spectral periods up to 3.0 s using the RESORCE dataset', *Bulletin of Earthquake Engineering*, 12(1), pp. 391–430. Available at: https://doi.org/10.1007/s10518-013-9525-5.

Bindi, D. *et al.* (2018) 'The pan-European engineering strong motion (ESM) flatfile: consistency check via residual analysis', *Bulletin of Earthquake Engineering*, pp. 1–20. Available at: https://doi.org/10.1007/s10518-018-0466-x.

Boore, D.M. *et al.* (2014) 'NGA-West2 Equations for Predicting PGA, PGV, and 5% Damped PSA for Shallow Crustal Earthquakes':, *Earthquake Spectra* [Preprint]. Available at: https://doi.org/10.1193/070113EQS184M.

Brune, J.N. (1970) 'Tectonic stress and the spectra of seismic shear waves from earthquakes', *Journal of Geophysical Research*, 75(26), pp. 4997–5009. Available at: https://doi.org/10.1029/JB075i026p04997.

Cauzzi, C. *et al.* (2015) 'Updated predictive equations for broadband (0.01–10 s) horizontal response spectra and peak ground motions, based on a global dataset of digital acceleration records', *Bulletin of Earthquake Engineering*, 13(6), pp. 1587–1612. Available at: https://doi.org/10.1007/s10518-014-9685-y.

Chiou, B.S.-J. and Youngs, R.R. (2014) 'Update of the Chiou and Youngs NGA Model for the Average Horizontal Component of Peak Ground Motion and Response Spectra':, *Earthquake Spectra* [Preprint]. Available at: https://doi.org/10.1193/072813EQS219M.

Hollender, F. *et al.* (2018) 'Characterization of site conditions (soil class, V_{S30}, velocity profiles) for 33 stations from the French permanent accelerometric network (RAP) using surface-wave methods', *Bulletin of Earthquake Engineering*, 16(6), pp. 2337–2365. Available at: https://doi.org/10.1007/s10518-017-0135-5.

Konno, K. and Ohmachi, T. (1998) 'Ground-motion characteristics estimated from spectral ratio between horizontal and vertical components of microtremor', *Bulletin of the Seismological Society of America*, 88(1), pp. 228–241.

Kotha, S.R. *et al.* (2020) 'A regionally-adaptable ground-motion model for shallow crustal earthquakes in Europe', *Bulletin of Earthquake Engineering*, 18(9), pp. 4091–4125. Available at: https://doi.org/10.1007/s10518-020-00869-1.

Lanzano, G. *et al.* (2019) 'The pan-European Engineering Strong Motion (ESM) flatfile: compilation criteria and data statistics', *Bulletin of Earthquake Engineering*, 17(2), pp. 561–582. Available at: https://doi.org/10.1007/s10518-018-0480-z.

Perron, V. *et al.* (2018) 'Selecting time windows of seismic phases and noise for engineering seismology applications: a versatile methodology and algorithm', *Bulletin of Earthquake Engineering*, 16(6), pp. 2211–2225. Available at: https://doi.org/10.1007/s10518-017-0131-9.

Wald, D.J. and Allen, T.I. (2007) 'Topographic Slope as a Proxy for Seismic Site Conditions and Amplification', *Bulletin of the Seismological Society of America*, 97(5), pp. 1379–1395. Available at: https://doi.org/10.1785/0120060267.